A High-Resolution Shear Velocity Model of the Crust and Uppermost Mantle beneath Westernmost Mediterranean including Radial Anisotropy

Lili Feng

CGG, Houston, TX 77072, USA

Corresponding author: Lili Feng (lili.feng@colorado.edu)

Key points:

- A 3-D radially anisotropic Vs model beneath Westernmost Mediterranean is constructed with surface waves and receiver functions.
- Isotropic Vsv structure captures several geological features, including the Iberian Massif, the Pyrenees, the Alboran slab and the Atlas Mountains.
- Crustal radial anisotropy identifies the extensional provinces, providing additional constraints to infer the Africa-Iberia movement during the Cenozoic Era.

Abstract

Using seismic data from 1186 stations deployed across the westernmost Mediterranean, I construct a high-resolution 3-D radially anisotropic model from a joint inversion of Rayleigh and Love wave dispersions, along with receiver functions. The Rayleigh and Love data are extracted from both ambient noise interferograms and earthquake waveforms, and a new three-station ambient noise interferometry method is used to further improve the data coverage. Features captured by the model include the following: (1) Crustal radial anisotropy identifies regions that have undergone extensional deformation, providing seismic constraints for a better understanding of the Africa-Iberia movement during the Cenozoic Era. (2) Crustal thickness map identifies regions with thick crust, including the Pyrenees, the Iberian Chain, the Gibraltar Arc and the Atlas Mountains. (3) The Iberian Massif is outlined as a high shear wave velocity block in the crust. (4) A sharp boundary between the Limousin and the Massif Central is imaged, low Vsv in the mantle beneath the Massif Central reflects remaining thermal signature of the magma. (5) The geometry of the Alboran slab is captured by the model, consistent with prediction from geodynamical modeling. (6) In the mantle beneath the Atlas Mountains, widespread low Vsv and positive radial anisotropy is observed, favoring the edge-driven convection (EDC) model explaining the lithospheric thinning.

Plain Language Summary

The Mediterranean is a unique place for geoscientists to investigate driving tectonic forces within a complex mobile belt. The tectonic and geodynamical history of the eastern and middle Mediterranean region since the late Eocene is relatively well documented, however, tectonic evolution of the westernmost Mediterranean remains debated. Using an unprecedented large seismic dataset, a new high-resolution Earth model is constructed using cutting-edge seismic imaging techniques, which utilizes waveform records extracted from both ambient seismic noise and earthquakes. The new model is overall consistent with existing Earth models, and also presents new insights to determine regions which have undergone extensional deformation. Identifying extensional provinces could further help geoscientists better reconstruct relative movement of the Africa plate and Iberian microplate, leading to an improved understanding of the dynamic evolution history of the western Mediterranean.

1. Introduction

1.1 Tectonic Background

Sitting between the Eurasian and the Africa plate, the Mediterranean region has experienced a complex tectonic evolution marked by oceanic lithosphere subduction and related crustal and mantle deformational processes. The region presents a variety of tectonic features and events, including arcuate belts, sedimentary basins, mountain edifices, active volcanoes and large earthquakes. The tectonic and geodynamical history of the eastern and middle Mediterranean region for the past ~ 35 Ma is relatively well investigated, as summarized by Faccenna et al. (2014). However, formation of several tectonic features located at the western Mediterranean (**Fig. 1b**) is still under debate. Indeed, the development of the Rif-Betic mountain belt could be explained by several hypotheses, including delamination or rolling back of the slab (e.g., Lonergan & White, 1997; Faccenna et al., 2004; Spakman & Wortel, 2004), change in subduction polarity (Vergés & Fernàndez, 2012) and extensional collapse (Platt et al., 1998; Molnar & Houseman, 2004). And the boundary of the westward extension of the Alboran region is estimated differently (e.g., Lonergan & White, 1997; Faccenna et al., 2004; Spakman & Wortel, 2004). It is widely agreed that the lithosphere beneath the Atlas Mountains is thin, however, the formation of shallow asthenosphere beneath the Atlas Mountains can be explained by different models, including a mantle plume which is part of the Canary system (e.g., Sun et al., 2014; Miller et al., 2015) and the edge-driven convection process (EDC, e.g., Kaslaniemi & van Hunen, 2014).

This study focuses on the westernmost Mediterranean (**Fig. 1b**), which consists of the southmost of France, the Iberian Peninsula and northern Morocco, separated by the Alboran Sea. The region is squeezed between the Eurasian and the Africa plate with compressive deformation occurring to the north at the Pyrenees and to the south at the Atlas Mountains. Indeed, GPS constraints on the Africa-Iberia plate boundary (Koulali et al., 2011) indicate that Betic zone of the southern Spain move west–southwest relative to Eurasia (~2–3 mm/yr) and Rif Mountains in the northern Morocco shows southwestward motion with respect to Africa (~3.5-4.0 mm/yr). The GPS velocities of the Pyrenees (e.g., Asensio et al., 2012) illustrate a southeastward motion with respect to the Eurasia.

During the Paleozoic, a variety of tectonic events have occurred to drive large continental blocks accreted to constitute the Pangea. The late Paleozoic orogeny of the Variscan and the Appalachian–Alleghanian belts resulted from the collision between Gondwana and Laurussia, and the Variscan orogeny is represented by the Iberian Massif in Spain. The Iberian Massif is the largest continuous exposure of pre-Permian rocks of the western part of the Iberian Peninsula (Fernández & Arenas, 2015). In Africa, Morocco presents almost all the Palaeozoic and Pre-cambrian outcrops of the northwestern Africa belonging to the Variscan orogeny (Michard et al., 2010). Starting in the Early-Middle Jurassic, Pangea began to rift as the Neo-Tethys Ocean opened, separating the Eurasian and Africa plate. The break-up of Pangea made Iberia became a microplate encompassed by sedimentary basins and water. The opening of the Atlantic Ocean occurred to the west of the Iberia as the Pangea broke up, which formed the Bay of Biscay as the Iberian microplate rotating counter-clockwise. The on-going convergence between the Africa and Eurasia plates was initiated in the Cretaceous. The Africa-Eurasia convergence has dominated the evolution of the Mediterranean basins and formation of several mountain ranges, including the Pyrenees, the Iberian Chains, the Betic-Rif Belt and the Atlas Mountains (Di Bucci et al., 2010; Laville et al., 2004; van Hinsbergen et al., 2014).

1.2 Previous tomographic studies

A comprehensive overview of geophysical research on Iberia and adjacent margins is recently presented by Diaz et al. (2021). Since the 1970's, numerous geoscientists have devoted their efforts to investigating the complex geological history of the Iberian Peninsula and surroundings with different geophysical approaches, and seismic tomography is one of the most important geophysical tools. Earliest regional tomographic models covering the region can date back to 1970s presented by Nolet (1977), in which the author used Rayleigh waves from a few seismic stations to infer upper mantle structure. More recent seismic studies imaging the crustal and mantle structure beneath the Mediterranean has been based on different approaches, including receiver functions (e.g., de Lis Mancilla & Diaz, 2015), surface wave tomography (e.g., Palomeras et al., 2017), body wave tomography (e.g, Bonnin et al., 2014) and full-waveform inversion (FWI) (e.g., Zhu & Tromp, 2013; Fichtner & Villaseñor, 2015). Most of the existing tomographic studies focuses on determination of isotropic structures, with a few exceptions. For instance, based on seismic data from 278 stations, Fichtner & Villaseñor (2015) determined Vsv/Vsh structures of the western Mediterranean using full-waveform inversion based on regional and local earthquake data. However, because the authors only used earthquake waveforms, which has lower signal-to-noise ratio at higher frequencies compared with ambient noise interferograms, the resolution of crustal anisotropy presented by Fichtner & Villaseñor (2015) may not be optimal. Indeed, as admitted by the authors, the inferred crustal anisotropy in Fichtner & Villaseñor (2015) may be strongly biased by event mislocation and near-field affect, producing artefacts of negative anisotropy associated with earthquake locations.

1.3 This study

In this study, I present a new 3-D radially anisotropic model of the crust and uppermost mantle beneath the westernmost Mediterranean, including southmost of France, the Iberian Peninsula and northern Morocco. The model is constructed by a Bayesian Monte Carlo joint inversion of Rayleigh and Love wave dispersions and receiver functions, with dispersion measurements extracted from both ambient noise and earthquake waveforms. This study uses a large seismic dataset from 1186 seismic stations deployed in and surrounding the westernmost Mediterranean (**Fig. 1**), including the IberArray (IB), the PYROPE array (X7), the PICASSO array (XB) and some other networks.

The principal novelty of this paper is the determination of a 3-D Vs model by jointly interpreting Rayleigh waves, Love waves and receiver functions, allowing me to simultaneously resolve 3-D Vsv structure in the crustal and uppermost mantle, crustal thickness, and radial anisotropy. This study is to some extent similar to Palomeras et al. (2017), in which the authors presented a 3-D lithospheric isotropic Vs model at similar region constructed by Rayleigh waves alone. However, there are four noteworthy differences. (1) To improve the ambient noise data coverage across the study region, I utilize a much larger seismic dataset with 1186 stations in total (**Fig. 1a**). In comparison, Palomeras et al. (2017) used 368 stations. Seismic stations distributed outside the study region (**Fig. 1b**) are used as virtual sources to improve the ambient noise data coverage, so that crustal structures could be better resolved. (2) Besides the fact that ~ 800 more stations are used, a newly-developed ambient noise three-station interferometry (Zhang et al., 2020; Feng, 2021) method is applied to further enhance the path coverage. The method could provide paths linking asynchronously deployed stations and could also yield interferograms with higher SNR than the traditional two-station interferograms. In addition, for the very first time, this study demonstrates that the three-station ambient noise interferometry could also be applied to the transverse-transverse (TT) components (before only used for ZZ components), so that Love waves can also be extracted. (3) Receiver functions are incorporated in this study, allowing me to better determine the Vs structures near the Moho and crustal thickness simultaneously. To the best of my knowledge, this is the first study constructing a Vs model for the study region by jointly interpreting receiver functions and surface waves. (4) Radial anisotropy (Vsh) across the study region is estimated by jointly interpreting Love waves in the inversion process. Extracting Love waves from ambient noise helps better constrain crustal radial anisotropy, which has not yet been done for the study region.

The Vsv structures resolved by the model are generally consistent with previous tomographic studies (e.g., Fichtner & Villaseñor, 2015; Palomeras et al., 2017). Besides, the newly inferred crustal anisotropy identifies regions may have undergone extensional deformation, providing seismic evidence for a better understanding of the relative Africa-Iberia movement during the Cenozoic Era. Uppermost mantle anisotropy helps us to better understand the dynamical processes beneath the Atlas Mountains.

2. Data and Methodology

2.1 Seismic Station Distribution

This study utilizes a seismic dataset including 48 permanent and temporary networks distributed within a distance of ~ 1500 km from the center of the Iberian Peninsula between January 2007 and April 2014 (**Fig. 1a**). The dataset includes 1186 broadband seismic stations in total, which is the most complete datasets ever used for seismic tomography across the westernmost Mediterranean.

The most important three networks are the IberArray (IB) deployed across the Iberian Peninsula, the PYROPE array (X7) covering the Pyrenees and surroundings, and the PICASSO array (XB) distributed at southern Spain and Morocco. Those three networks include 459 stations and they are identified with blue, red and green colors in **Figure 1.** Other networks are colored in yellow. **Table S1** summarizes all the seismic networks and associated DOI.

2.2 Ambient Noise Tomography

2.2.1 Two-station interferometry

Continuous seismic waveforms are routinely processed with the two-station ambient noise interferometry method, namely, noise correlation (Bensen et al., 2007; Ritzwoller & Feng, 2019) to construct two-station interferograms which include surface wave arrivals. Rayleigh wave dispersions can be extracted from the vertical-vertical (ZZ) component interferograms and Love wave phase arrivals are retrieved from the transverse- transverse (TT) component.

2.2.2 Three-station direct wave interferometry

To further enhance surface wave data coverage at short periods, so that the crustal structures can be better resolved, a recently developed three-station direct wave interferometry technique is applied (Zhang et al., 2020). Both the ZZ and TT component two-station interferograms are used to construct the three-station interferograms as supplementary datasets to improve path coverage. The three-station interferometry workflow is directly taken from Feng (2021), which is slightly different from Zhang et al. (2020)'s approach.

Previous studies of three-station direct wave interferometry only applied the technique to ZZ component interferograms (Feng, 2021; Zhang et al., 2020), this study extends the usage of the three-station method to TT components so that Love wave data coverage can also be improved, resulting in more reliable determination of crustal radial anisotropy.

Incorporating three-station interferograms as additional dataset for surface wave tomography has two advantages. (1) Asynchronous interferograms between stations that are not deployed simultaneously could be constructed. **Figure 2a and 2b** show a subset of the ZZ and TT component asynchronous interferograms, with SNR larger than 15 (ZZ) or 10 (TT). For those asynchronous interferograms, at least one station belongs to the IB, XB or X7 networks. As marked on the figures, the three-station interferograms provide > 62,000 additional paths for Rayleigh waves linking the IB, XB, or X7 stations with other networks, and > 38,000 additional paths for Love waves. (2) Three-station interferograms typically yield surface wave phase arrivals with higher SNR ratio, as demonstrated by Feng (2021) and Zhang et al. (2020) and also illustrated by the sample interferograms in **Figure 2c and 2d**.

Automatic frequency-time analysis (FTAN) is applied to both two- and three-station interferograms to measure the dispersive arrivals of surface waves, yielding Rayleigh wave dispersion curves of periods 8 – 50 s and Love wave measurements of 8 – 40 s. Then I apply the eikonal tomography (Lin et al., 2009) to determine 2-D phase speed maps for Rayleigh and Love waves.

2.3 Earthquake Tomography

Eikonal tomography is also applied to dispersion measurements extracted from teleseismic earthquake waveforms (ISC catalog, 2007 – 2014, M_s > 5.5), for both Rayleigh and Love waves at periods of 26 s – 50 s. Above 50 s period (Rayleigh wave only), Helmholtz tomography is performed to take into account finite frequency effect (Lin & Ritzwoller, 2011). Rayleigh wave earthquake phase speed maps are produced at periods of 26 s – 85 s, while Love wave maps do not extend to periods longer than 50 s. The final phase velocity maps are constructed by combining ambient noise and earthquake results.

2.4 Receiver Function Analysis

In order to better determine crustal thickness, receiver functions are computed in this study. An iterative deconvolution algorithm (Ligorria & Ammon, 1999) is applied to teleseismic P wave arrivals from earthquakes with M_w>5.5 and epicentral distances between 30°- 120°, producing radial component P-wave receiver functions. Then a harmonic stripping approach (Shen et al., 2012) is applied to remove the impact of azimuthal anisotropy and dipping interface, resulting in the isotropic component of P-wave receiver function. The isotropic P-wave receiver function is the final product of receiver function to be used for the joint inversion.

3. Rayleigh and Love wave phase speed maps

In **Figure 3**, I present sample phase speed maps for both Rayleigh and Love waves. Several geological structures can be identified at different periods and here I list a few notable examples.

(1) The Iberian Massif emerges as a large-scale high-velocity block at shorter periods (T = 10 and 20 s) for both Rayleigh and Love waves.

(2) The locations of the Alentejo-Guadalquivir Basin, the Rabat Basin and the Rif Basin are captured with extremely low speed at all the periods except T = 70 s Rayleigh wave map. The low-speed anomaly at those locations reflects slow Vsv/Vsh structure in the sediments at shorter periods (T < ~20 s), while the low velocity at intermediate periods (T = 30 – 50 s) indicates thick crust.

(3) The Pyrenees is identified with relatively high speed at T = 10 s Rayleigh wave map, but it becomes a low velocity stripe in the T = 30 s Rayleigh wave map.

(4) The Iberic Chain and surroundings are imaged with relatively low speed in the T = 20 s and 30 s period Rayleigh wave map.

(5) At longer periods (> 40 s), Rayleigh wave maps identify slow speed anomaly at the Atlas Mountains.

(6) There is a sharp velocity contrast near the Toulouse Fault in longer periods (> 40 s) Rayleigh wave speed maps.

(7) At 70 s period, high-speed anomaly near the Alboran Sea is resolved in the Rayleigh wave map.

Rayleigh and Love wave phase speed maps, along with receiver functions, are the input for the Bayesian Monte Carlo inversion to infer shear wave velocity structure with radial anisotropy.

4. Bayesian Monte Carlo Inversion

A Bayesian Monte Carlo inversion is performed to construct a 3-D anisotropic Vs model, on a regular geographical grid with spacing of ~ 20 km (0.2° by longitude and latitude). Input for the Bayesian inversion includes local Rayleigh and Love wave dispersion curves taken from phase speed maps, along with receiver functions. The inversion workflow is taken from Shen et al. (2012), Feng & Ritzwoller (2019) and Feng (2021), which naturally takes into account the reference model and additional prior constraints. In the following subsections, I briefly summarize the model parameterization, reference model, prior constraints, Monte Carlo sampling procedure, and finally, construction of a final 3-D model. More technical details can be found in Feng & Ritzwoller (2019) and Feng (2021).

4.1 Model parametrization and perturbation ranges

At each inversion grid point, a radially anisotropic Vs profile (0-200 km) is fully described by 15 model parameters. The allowed perturbation ranges for each parameter are defined based on the reference models (CRUST-1.0 and ak135 model).

1. Sedimentary layer (Vsv), 3 parameters: Three parameters are used to determine sedimentary structure, including Vsv at the top and bottom of the sediments along with sedimentary thickness. Vsv at intermediate depth inside the sedimentary basins increase linearly with depth. Vsv values can vary from 0.2 km/s to 2.5 km/s and the sedimentary thickness is allowed to perturb from 0 to twice of the reference value. The reference thickness is taken from the CRUST-1.0 model (Laske et al., 2013).
2. Crystalline crust (Vsv), 5 parameters: Vsv inside the crystalline crust is defined by four cubic B-splines. The corresponding B-spline coefficients are model parameters to be determined from the inversion. In addition, crustal thickness is another model parameter that needs to be inferred. The Vsv values in the crystalline crust are allowed to vary $\pm 20\%$ with respect to the reference values taken from the 1-D ak135 model (Kennett et al., 1995). The crustal thickness varies by $\pm$ 80% around reference value m_0 taken from the CRUST-1.0 model (Laske et al., 2013).
3. Mantle (Vsv), 5 parameters: Mantle Vsv structure is determined by five cubic B-splines. Therefore, five B-spline coefficients need to be inferred by the inversion.
4. Radial anisotropy (γ), 2 parameters: The shear wave radial anisotropy, is the difference in propagation wave velocity between horizontally (Vsh) and vertically (Vsv) polarized shear waves. The strength of the radial anisotropy, γ, is defined as

$$\gamma = \frac{(V_{sh} - V_{sv})}{V_s} \tag{1}$$

where $V_s = (V_{sh} + V_{sv})/2$. Similar to Feng & Ritzwoller (2019), I use a simple parameterization for radial anisotropy. Namely, the radial anisotropy is assumed to be vertically uniform in the crystalline crust and mantle respectively. The strength of crustal (γ_c) and mantle (γ_m) radial anisotropy are allowed to perturbed $\pm$ 10%. As shown by **Figure 7b**, such a simple two-layer anisotropic model suffices to fit data at most places.

Table S2 summarizes the range of each model parameter.

4.2 Additional prior constraints

To exclude physically unrealistic models, additional prior constraints are implemented in the inversion process (Feng & Ritzwoller, 2019), including: (1) Velocity jumps in both Vsv and Vsh are positive at each Earth's interface. (2) Vsv and Vsh are constrained to be less than 4.3 km throughout the crust. (3) In the crust, Vsv and Vsh monotonically increase with depth. (4) Vsv and Vsh are constrained to be in the range of 4.0 km/s ~ 4.6 km/s at the shallowest layer in the mantle. (5) Vsv and Vsh are not allowed to exceed 4.9 km/s at all depth ranges. (6) Vsv and Vsh are larger than 4.3 km/s at 200 km depth (bottom of the model). (7) To discourage spurious vertical oscillations in the mantle, the difference at the local maxima and minima in Vsv and Vsh cannot exceed 10 m/s.

The additional prior constraints help excluding nonphysical models, and they also have an impact on the prior distribution. Indeed, as shown in **Figure S1**, the prior distributions of model parameters are non-uniform due to the model parameterization and additional prior constraints.

4.3 Posterior Distributions

Posterior distributions of the model parameters are produced from the Markov Chain Monte Carlo (MCMC) sampling process based on data fitness. A model is accepted to construct the posterior distribution if its corresponding data misfit is smaller than $\chi_{min} + 0.5$, where χ_{min} is the misfit value of the model the best fitting the Rayleigh and Love wave dispersion, along with receiver function. Details about the MCMC sampling process can be found in Shen et al. (2012), Feng & Ritzwoller (2019) and Feng (2021). Example posterior marginal distributions of Vsv at 15 and 80 km depths, along with crustal thickness, are presented in **Figure S1**.

4.4 Constructing 3-D model

At each station inside the study region, a Bayesian Monte Carlo inversion is performed based on Rayleigh and Love wave phase speed curves along with receiver functions. However, as shown in **Figure 3**, both Rayleigh and Love wave phase speed maps extend to offshore region where receiver functions are not available. To make the final 3-D model cover the offshore area, I perform another group of inversions on a regular geographical grid with spacing of ~ 20 km (0.2° by longitude and latitude), using surface wave dispersion data only. Then, using Shen et al. (2018)'s and Feng (2021)'s approach, a final radially anisotropic Vs model is obtained by merging the station-based model with the grid-point based model.

5. Results

The output of the Bayesian Monte Carlo inversion is a 3-D shear wave velocity model with radial anisotropy, extending to a maximum depth of 200 km.

5.1 Crustal Vsv

Figure 4a, 4b and 4c present Vsv slices in the crust, at three sample depths of 3 km, 10 km and 20 km (central-depth $\pm 3\ km$). The locations of major sedimentary basins are captured in the 3 km slice, including the Aquitaine Basin located north to the Pyrenees; the Alentejo-Guadalquivir Basin covering the Gulf of Cadiz; the Rabat Basin west to the Rif mountains; and the Rif Basin located at Rif but also extends offshore to the Alboran Sea (Pawlewicz et al., 1997). The Iberian Massif emerges as a relatively high-speed anomaly at 3 km depth and its boundary is well captured by the model. At 10 km depth, both the Pyrenees and the Iberian Chain are imaged as relatively high-velocity stripes, and the high-speed anomaly representing the Iberian Massif becomes more prominent. The Betic-Rif Belt and surroundings emerge with extremely slow Vsv. Going deeper to 20 km depth, the Pyrenees high-speed stripe disappears while the Iberian Chain stripe, the Iberian Massif and the Betic-Rif Belt anomaly can still be identified. Extremely high Vsv beneath Alboran Sea emerges, indicating shallow Moho at this location.

5.2 Crustal Thickness

Figure 5b is a crustal thickness map constructed in this study. I also present the PRISM3D crustal thickness (Arroucau et al., 2021) as **Figure 5a** for comparison. Probably because the PRISM3D model is essentially an average model produced from a variety of different existing seismic models, the map looks generally smoother than the crustal thickness map constructed in this study. However, the overall patterns are generally consistent, as both maps identify relatively thick crust at Pyrenees, the Cantabrian Range, the Iberian Chain, the Gibraltar Arc and the Atlas Mountains. Besides, very thin crust is resolved beneath the Alboran Sea and the Bay of Biscay in both models.

5.3 Mantle Vsv

To illustrate Vsv distribution in the mantle, three sample Vsv slices at 60 km, 80 km and 100 km depths (central-depth $\pm 3\ km$) are presented as **Fig. 4d, 4e and 4f**. The Massif Central, located at the northeastern corner of the map, is resolved as a low-Vsv anomaly whose western boundary is defined by the Toulouse Fault. West to the Toulouse Fault, the Limousin emerges with extremely high Vsv, probably indicating a rigid lithospheric domain. At 60 km depth, the western part of the Pyrenees has relatively low Vsv than its surroundings, while the slightly low-Vsv region changes its distribution at 80 km and 100 km depths. The Iberian Massif emerges with a variant distribution of Vsv in the 60 km map, however, moving deeper to 100 km depth, the Iberian Massif is resolved with low Vsv. High Vsv is imaged beneath the Gibraltar Arc at all depth slices in the mantle. In Morocco, a relatively uniform low-speed block emerges beneath the Atlas Mountains and surroundings, indicating thin lithosphere.

5.4 Radial Anisotropy

Crustal (γ_c) and mantle (γ_m) radial anisotropy maps are illustrated in **Fig. 6a and 6b**. γ_c are considered indeterminate if the one standard deviation uncertainty is larger than 1.5 %. In the mantle, uncertainties larger than 2 % are considered as indeterminate. The grid points with indeterminate anisotropy are shown in grey color. Most of the regions across the study area emerge with positive anisotropy in the crust and mantle, with very few exceptions. Locations with high elevations are generally associated with relatively smaller crustal anisotropy than their surrounding regions, including the Pyrenees and the Iberian Chain. However, one exception with high elevation but also strong crustal anisotropy is the Betic mountains. In the mantle, the Northern Plateau and central eastern part of the Iberian Peninsula are identified with relatively large anisotropy. Strong mantle anisotropy also emerges beneath the Atlas Mountains and surroundings.

6. Discussion

In this section, I quantitatively analyze the reliability of the anisotropic part of the model, and also discuss the geological and tectonic implications from the model.

6.1 Model Assessment: Reliability of the Inferred Anisotropy

It is well-known that the inference of anisotropy is typically more difficult than imaging isotropic structures (Vsv). This is mainly because anisotropy only has a second-order impact on observations, and hence unreal features can be produced by overfitting the data. To assess the reliability of the estimated radial anisotropy, it is desirable to perform inversions with different model parameterizations to investigate the variance reductions.

As illustrated by **Figure S1b, S1h, and S1n**, Love wave dispersion curves cannot be reasonably fitted with isotropic profiles at the three sample stations. This is the well-known phenomenon called “Rayleigh-Love discrepancy”. Namely, an isotropic Vs model cannot reasonably fit both

Rayleigh and Love wave dispersion data. As shown by **Figure 7a**, an isotropic model produces widespread large misfit values across the study region, indicating the fact that the Rayleigh-Love discrepancy is broadly observed in the study region.

To resolve the Rayleigh-Love discrepancy, radial anisotropy is required. Radial anisotropy, also called polarization anisotropy (e.g., Moschetti et al., 2010), refers to the phenomenon that vertically polarized S waves (V_{sv}) have different wave speed compared with horizontally polarized S waves (V_{sh}). Because Rayleigh waves are mostly sensitive to V_{sv} and Love waves are dominantly controlled by V_{sh}, therefore, the Rayleigh-Love discrepancy typically indicates existence of strong radial anisotropy ($V_{sv} \neq V_{sh}$).

As shown in **Figure S1b, S1h, and S1n**, by allowing radial anisotropy in the crust and mantle, Love wave dispersion curves can be fitted at all the sample stations. Moschetti et al. (2010) and Feng & Ritzwoller (2019) showed that there is a negative trade-off relationship between crustal and mantle anisotropy. Indeed, as illustrated by **Figure S1f, S1l, and S1r,** negative trade-offs between the crustal and mantle anisotropy are observed at all sample locations. The inferred amplitudes of both crustal and mantle anisotropy could be affected by the trade-off and thus special care much be taken when building a radial anisotropy model. The anisotropy trade-off naturally raises a question: Do we really need both crustal and mantle anisotropy to fit the data?

To answer this question, I perform two additional inversions, one only allows radial anisotropy in the crust and another with anisotropy confined in the mantle. **Figure 7c and Figure 7d** show the misfit maps corresponding to the mantle anisotropy only and crustal anisotropy only inversions. By inspecting the misfit maps, three conclusions can be drawn:

(1) Incorporating anisotropy in the crust or mantle can improve data fitness and partially resolve the Rayleigh-Love discrepancy (**Figure 7c and Figure 7d**), while the best data fitting is achieved by allowing both crust and mantle to be anisotropic (**Figure 7b**).

(2) The patterns of the crustal and mantle misfit maps (**Figure 7c and Figure 7d**) are generally similar to the crustal and mantle anisotropy maps (**Figure 6**). The similarities imply that inferred anisotropy is indeed required by the data.

(3) Crustal anisotropy improves the variance reduction more than the mantle anisotropy, this implies that crustal anisotropy is determined more reliably. Indeed, as also shown by the

anisotropy trade-off figures (**Figure S1f, S1l, and S1r**), non-zero crustal anisotropy is generally required by almost all the accepted models.

The advantage of the Bayesian Monte Carlo inversion is that uncertainties of model parameters are produced, which could be naturally used as references to tell us how much we should believe the model or which part of the model is more believable. The uncertainty estimates are used to identify indeterminate grid points in **Figure 6**, in which crustal anisotropy is considered indeterminate if the associated uncertainty is > 1.5 % and an uncertainty threshold value of 2 % is used to identify indeterminate points in the mantle anisotropy map.

As a summary, I conclude that the anisotropic part (γ) of the model is overall reliable and justified by the data. Because crustal anisotropy improves the variance reduction more, hence it is more reliable than the inferred mantle anisotropy.

6.2 Massif Central and Pyrenees

In the mantle, the Massif Central is imaged as a low Vsv anomaly whose western boundary coincides with the Toulouse Fault, as shown by three sample Vsv depth slices (**Fig. 4d, 4e and 4f**) and the vertical cross-section A-A' (**Fig. 8**). The terrane has relatively thin crust (**Fig. 5b**) and there is widespread positive radial anisotropy in the mantle (**Fig. 6b**). The Massif Central has experienced strong crustal thinning and intense volcanism (Perrier & Ruegg, 1973), which are confined only to the east of the Toulouse Fault. The terrane is also associated with a large negative Bouguer anomaly, which indicates the existence of a low-density block at the depth ~ 50 km. Existing P-wave tomographic studies (e.g., Granet et al., 1995; Chevrot et al., 2014) also reported the Massif Central as a low-speed anomaly, which reflects the remaining thermal signature of the magma that distributed through the lithosphere. A plume-type structure beneath the lithosphere is suggested by previous studies (e.g., Granet et al., 1995), while the depth origin of the plume is still an open question. The plume model is overall consistent with broad distribution of Vsv in this region, while less compatible with the positive radial anisotropy at this location. It may imply that the observed radial anisotropy in this region mainly reflects the fossil anisotropy confined in the lithosphere.

The Pyrenees emerges as a high Vsv stripe at ~ 10 km depth (**Fig 4b**), with the fastest Vsv distributed at the western Pyrenees. In the mantle, relatively low Vsv at 60 km depth is imaged beneath the western Pyrenees (**Fig. 4d**), which agrees well with Fichtner and Villasenor (2015)'s full waveform inversion model while less consistent with Chevrot et al. (2014)'s Vp model. Eastern Pyrenees is captured with high Vsv at 60 km depth, which is also identified as a pronounced high Vp anomaly in Chevrot et al. (2014)'s model. The fast speed in the eastern Pyrenees may suggest a colder European lithosphere, which is consistent with lager convergence to the east than the west of the mountain range (Teixell, 1998). Chevrot et al. (2014) suggested that the contrasting thermal state of the lithosphere along the Pyrenees could also be explained by a more intense Cretaceous extensional deformation to the west (Jammes et al., 2009), which, however, is not quite supported by relatively lower crustal radial anisotropy (**Fig. 6a**) distributed along the mountain range.

6.3 Iberian Peninsula

The Variscan Iberian Massif is outlined as a distinct block in the crust with high Vsv values (**Fig. 4a, 4b and 4c**). The boundary of the Massif is better captured at shallowest depth (**Fig. 4a**) compared with existing models (e.g. Palomeras et al., 2017), implying higher resolution of the model presented in this study. The high shear wave velocity in this Variscan domain may reflect large number of granitic intrusions, which differentiates itself with the Alpine deformation structures such as the Pyrenees, Betics, Central system and Iberian orogen. The crustal thickness of the Iberian Massif is relatively small, with values around 25 ~ 30 km (**Fig. 5b**). In contrast, the Iberian Chain, formed during the Alpine orogeny, is characterized by thicker crust.

In the uppermost mantle, northern part of the Iberian Massif is imaged with relatively low Vsv (**Fig. 4d, 4e and 4f**, and cross-section B-B'), implying a thin lithosphere. Indeed, heat flow measurements at this area is unusually high (> 150 mW m^{-2}, Fernandez et al., 1995), which could be explained by thinner lithosphere, large temperature gradient and high heat flow. More prominent low Vsv in the mantle is found at the north of the Betic Moutains, which is the Calatrava Volcanic field. The large reduction in Vsv (~ 6 %) beneath the volcanic field and surroundings is larger than typical Vsv drop from a dry depleted lithosphere to a hydrated, fertile asthenosphere (Schutt and Lesher, 2006; Palomeras et al., 2017). To fully explain the low Vsv, a temperature drop of ~ 300 K (Cammarano et al., 2003), or close to 1 % of partial melting (Hammond & Humphreys, 2000) is required. The LAB (Lithosphere-Asthenosphere Boundary) beneath the Calatrava Volcanic field is likely to be even thinner than northern part of the Iberian Massif (cross-section C-C' in **Fig. 8**).

6.4 Gibraltar Arc

The Gibraltar Arc region, covered by unmetamorphosed marine Meso-Cenozoic sedimentary sediments (**Fig. 4a**), is identified with extremely low crustal Vsv (**Fig. 4b and Fig. 4c**) and thick crust (**Fig. 5b**), consistent with existing tomography and receiver function studies (e.g., Palomeras et al., 2017; de Lis Mancilla & Diaz, 2015). Beneath the region with thick crust, high Vsv is found in the mantle which indicate the location and geometry of the Alboran slab (**Fig. 4d, 4e and Fig. 4f**).

Two vertical cross-sections (B-B' and D-D') in **Figure. 8** represent the vertical cross view of the Alboran slab system from different perspectives. Existing geodynamical modeling study (Chertova et al., 2014) reconstructs the movement of the Alboran slab and the authors favored a scenario (called scenario S1 in Chertova et al., 2014) presenting a N-W dipping subduction initially confined to the Balearic margin at ~35 Ma. The scenario S1 produces a present-day slab morphology which is consistent with my model. It indicates that the slab rolled back to the north African margin in the Middle Miocene (15 Ma) and was almost in its current position in the Tortonian (10–8 Ma). The Vsv distribution in the mantle presented in cross-section D-D' in **Figure. 8** depicts the very top part of the rollback slab geometry. The slab rollback has initiated delamination of the continental lithosphere beneath the Gibraltar Arc, suggested by several previous studies (e.g., Turner et al., 2014; Palomeras et al., 2017). Indeed, unusually thick crust (**Fig. 5b**) beneath the Rif-Betic Belt may be caused by a depression of the continental lithosphere resulting from the load of the descending slab, which could be enough to initiate delamination of the lower crust and lithosphere (Valera et al., 2008). The mechanism of the subduction driven delamination is also justified by the age of the sedimentary basins covering the Rif-Betic Belt (**Fig. 4a**, Palomeras et al., 2017), as the Pre-Betic basins started to form in late Miocene (~11 Ma) and uplift progressed to the west (Irribarren et al., 2009).

6.5 Atlas Mountains

Widespread low Vsv (**Fig. 4d, 4e and 4f**), along with thick crust (**Fig. 5b**), have been found beneath the Atlas Mountains. Thin lithosphere has been suggested by several studies (e.g., Palomeras et al., 2017) to explain its high elevations and strong positive geoid anomaly (e.g., Fullea et al., 2010). By assuming the existence of very thin lithosphere, it is natural to conclude that the strong radial anisotropy (**Fig. 6b**) in the mantle dominantly reflects the contribution from the asthenosphere, which may further provide implications to the dynamical processes beneath this region.

In the mantle, the dominant cause of anisotropy is the lattice-preferred orientation (LPO) of olivine fabrics (Montagner, 2007), as olivine is the most common upper mantle mineral with a strong single crystal anisotropy. Under different physical and chemical environments (e.g., pressure, temperature, water contents), different types of olivine fabrics can develop and the resulting radial anisotropy could differ in both magnitude and patterns. For A- and E-type olivine, the fast axes of the olivine crystals align in the direction of shear deformation and thus could be used as an indicator of mantle flow pattern (Karato et al., 2008). Under the assumption of A- or E-type olivine, a positive radial anisotropy ($V_{sh} > V_{sv}$) in the mantle indicates horizontal flow while a negative anisotropy ($V_{sh} < V_{sv}$) implies vertical flow (Karato et al., 2008).

Several existing studies proposed that a mantle plume, which is part of the Canary system, is responsible for the lithospheric thinning beneath the Atlas Mountains (e.g., Sun et al., 2014; Miller et al., 2015), which is not quite consistent with my model due to the presence of positive radial anisotropy in the asthenospheric mantle. An alternative mechanism which explains the lithospheric thinning and mantle melting is the edge-driven convection (EDC, e.g., Kaslaniemi & van Hunen, 2014). The lithospheric thickness gradient from the West African Craton to the delaminated lithosphere near the Gibraltar Arc may have triggered secondary EDC beneath the Atlas Mountains, which may further create shear asthenospheric flows producing positive radial anisotropy ($V_{sh} > V_{sv}$, **Fig. 7b**). The observed anisotropy is consistent the EDC model, and the low Vsv imaged in the mantle (**Fig. 4d, 4e and 4f,** cross-section B-B' **in Fig. 8**) may reflect the partial melting produced by the depression in the EDC cells. The EDC model can also explain the volcanism with 20 Ma quiet gap in the middle and the piecewise delamination of the lithosphere under the Atlas Mountains (Kaslaniemi & van Hunen, 2014).

6.6 Identifying Extensional Provinces with Crustal Anisotropy

Figure 6a shows that positive crustal anisotropy is broadly distributed across the westernmost Mediterranean, with very few exceptions associated with very weak negative radial anisotropy ($V_{sv} > V_{sh}$). I focus on the interpretation of positive anisotropy in this subsection.

Widespread positive crustal radial anisotropy has been reported at different locations of the Earth, including the Basin and Range Province (e.g., Moschetti et al., 2010), Alaska (e.g., Feng &

Ritzwoller, 2019) and Tibet (e.g., Shapiro et al., 2004). Existing studies typically attribute the observed crustal anisotropy to the LPO (lattice-preferred orientation) of mica-rich foliated metamorphic rocks because they are abundant in the crystalline crust. Besides, laboratory experiments (e.g., Lloyd et al., 2009) have shown that single crystal mica is one of the most anisotropic crustal minerals. The laminated sheets of single crustal mica making it possible to describe the crystal as transversely isotropic (TI) media, also called hexagonal symmetric media in some previous studies (e.g., Xie et al., 2015). The TI media has a symmetry axis and can be fully described by five elastic parameters if the alignment of the symmetry axis is assuming vertically oriented. The TI assumption remains a valid approximation for a variety types of mica-rich rock samples (e.g., Lloyd et al., 2009; Brownlee et al., 2017). Another possible candidate that may also play an important role contributing to the observed seismic anisotropy is amphibole (e.g., Tatham et al., 2008). However, single crystal amphibole has weaker anisotropy than mica and the rock samples abundant in amphibole typically exhibit as orthorhombic media (Brownlee et al., 2017), which could not be described by radial anisotropy. Other continental crustal minerals that may contribute to seismic anisotropy are quartz and feldspars, but in a destructive way. Experimental results (e.g., Ward et al., 2012) have shown that quartz and feldspars are not likely to produce a LPO induced anisotropy but could dilute the anisotropic strength of the mica-bearing rocks. As a summary, the observed anisotropy (**Figure 6a**) most likely originates from the mica-rich rocks, however, it is hard to rule out the contribution from other types of crustal composition.

Despite of the complexity in the composition of the anisotropic rocks, the relationship between strong radial anisotropy and crustal deformation is probably more straightforward. For example, Shapiro et al. (2004) reported that the radial anisotropy is largely controlled by channel flow in the mid-to-lower crust in Tibet, which is associated to crustal thinning. Similar relationship between radial anisotropy and crustal thinning has been found at the Basin and Range Province by Moschetti et al. (2010), in which the authors reported that the observed widespread radial anisotropy is mostly confined to the region undergone significant extension during the Cenozoic Era. However, the relationship between radial anisotropy and crustal thinning may not always be valid. For instance, in Alaska, Feng & Ritzwoller (2019) reported that the radial anisotropy is strong at the southern parts of the Brooks Range, the Yukon composite Terrane, the Seward Peninsula and the Ruby Terrane. These places have been identified as regions undergone significant mid-Cretaceous extension, which were called as the “hinterland” by Miller & Hudson

(1991). Although relatively thin crust has been found at the Yukon composite Terrane, the Seward Peninsula and the Ruby Terrane, however, thick crust beneath the Brooks Range has reported by Feng & Ritzwoller (2019) and receiver function studies (e.g., Miller & Moresi, 2018). In a nutshell, strong radial anisotropy in the crust is generally associated with extensional deformation, it may also be related to relatively thin crust and low topography, but there are exceptions (e.g., Feng & Ritzwoller, 2019).

The crustal anisotropy map (**Fig. 6a**) approximately identifies locations with Cenozoic and Mesozoic-Cenozoic outcrops (Arroucau et al., 2021), which indicates that those regions may have undergone extensional deformation during Mesozoic or Cenozoic Era. Strong crustal anisotropy is overall associated with thinner crust (**Fig. 5b**), with one exception beneath the Betic mountains. To better locate the areas with strong crustal radial anisotropy, I produce a map (**Figure 6c)** identifying regions with relatively strong crustal anisotropy in blue ($\gamma_c > 3.5\%$).

De Vincente et al. (2009) presented a tectonic model reconstructing the Africa-Iberia movement during the Cenozoic Era. From the early Oligocene to lower Miocene, the paleo-reconstructions (Rosenbaum et al., 2002) indicated that the Africa plate and the Iberian microplate came 115 km closer. Compressive deformation (shortening) was transmitted to the interior of the plates leading to most topographical features of the Iberian Peninsula and Morocco, including the Pyrenees, the Iberian Chain, the Central Range, the Cantabrian Range and the Atlas Mountains. These mountain ranges are associated with weaker crustal anisotropy (< 3.5%, **Fig. 6a and Fig. 6c**). Possible shortening locations from the early Oligocene to the lower Miocene are marked with red arrows in **Figure 6c**. The red arrow areas (shortening, associated with topographical features) and the blue regions (extension, inferred from crustal anisotropy) constitute a "jigsaw fit" as a whole, which means that the crustal anisotropy distribution is consistent with De Vincente & Vegas (2009)'s model explaining the Cenozoic movement of the African plate and the Iberian microplate.

The only outliner which does not really fit in the above "jigsaw fit" is the Betics. However, as Turner et al. (2014) suggested and also discussed earlier in section 6.4, the load on the continental margin resulting from the Alboran slab is depressing the Moho beneath the Rif-Betic Belt, triggering detachment of lithosphere and allowing the asthenosphere to flow in to replace the lithospheric materials. Unlike topographical features formed by compression, the uplift of the Betics is produced by the flow-in asthenospheric material at the subcrustal depth, which may be accompanied by crustal extension (Huismans & Beaumont, 2008) to produce strong radial anisotropy.

7. Conclusions

In this study, I present a new 3-D radially anisotropic shear wave velocity model for the crust and uppermost mantle to a depth of 200 km beneath the westernmost Mediterranean, including southmost of France, the Iberian Peninsula and northern Morocco. The model is constructed from a joint Bayesian Monte Carlo inversion of Rayleigh and Love wave dispersion curves along with receiver functions. The Vsv structures imaged by the model are generally consistent with existing tomographic models (e.g., Fichtner & Villaseñor, 2015; Palomeras et al., 2017) and the crustal thickness map indicates thick crust associated with major mountain ranges. Radial anisotropy in the crust identifies regions that have undergone extensional deformation in the past, which may help us better reconstruct the Africa-Iberia movement from the early Oligocene to the lower Miocene, leading to an improved understanding of the Cenozoic evolution of the western Mediterranean.

The anisotropic 3-D Vs model is a useful reference for a variety of purposes. It can be used as a reference for better understanding of the tectonic evolution of the westernmost Mediterranean and can also help predicting other types of seismic data, such as seismic amplification (Feng & Ritzwoller, 2017). In the future, incorporating observations from azimuthal anisotropy to infer a titled-TI model (e.g., Xie et al., 2015) is desirable, which could lead to an improved understanding of the deformational processes beneath this region.

Acknowledgments

The author is grateful to several data centers (IRIS, ORFEUS, GEOFON, RESIF) which make their data available to the public. The network codes for data and corresponding DOI can be found in **Table S1**. He also thanks Weisen Shen at Stony Brook University for providing computational facilities for the data processing of this work.

References

Arroucau, P., Custódio, S., Civiero, C., Silveira, G., Dias, N., Díaz, J., Villaseñor, A. and Bodin, T., 2021. PRISM3D: a 3-D reference seismic model for Iberia and adjacent areas. *Geophysical Journal International*, *225*(2), pp.789-810. https://doi.org/10.1093/gji/ggab005

Asensio, E., Khazaradze, G., Echeverria, A., King, R.W. and Vilajosana, I., 2012. GPS studies of active deformation in the Pyrenees. *Geophysical Journal International*, *190*(2), pp.913-921. https://doi.org/10.1111/j.1365-246X.2012.05525.x

Becker, T.W., Kustowski, B. and Ekström, G., 2008. Radial seismic anisotropy as a constraint for upper mantle rheology. *Earth and Planetary Science Letters*, *267*(1-2), pp.213-227. https://doi.org/10.1016/j.epsl.2007.11.038

Bensen, G.D., Ritzwoller, M.H., Barmin, M.P., Levshin, A.L., Lin, F., Moschetti, M.P., Shapiro, N.M. and Yang, Y., 2007. Processing seismic ambient noise data to obtain reliable broad-band surface wave dispersion measurements. *Geophysical Journal International*, *169*(3), pp.1239-1260. https://doi.org/10.1111/j.1365-246X.2007.03374.x

Bonnin, M., Nolet, G., Villasenor, A., Gallart, J. and Thomas, C., 2014. Multiple-frequency tomography of the upper mantle beneath the African/Iberian collision zone. *Geophysical Journal International*, *198*(3), pp.1458-1473. https://doi.org/10.1093/gji/ggu214

Brownlee, S. J., Schulte-Pelkum, V., Raju, A., Mahan, K., Condit, C., & Orlandini, O. F., 2017. Characteristics of deep crustal seismic anisotropy from a compilation of rock elasticity tensors and their expression in receiver functions. *Tectonics*, 36, 1835–1857. https://doi.org/10.1002/2017TC004625

Cammarano, F., Goes, S., Vacher, P. and Giardini, D., 2003. Inferring upper-mantle temperatures from seismic velocities. *Physics of the Earth and Planetary Interiors*, *138*(3-4), pp.197-222., doi:10.1016/S0031-9201(03)00156-0.

Chevrot, S., Villaseñor, A., Sylvander, M., Benahmed, S., Beucler, E., Cougoulat, G., Delmas, P., De Saint Blanquat, M., Diaz, J., Gallart, J. and Grimaud, F., 2014. High-resolution imaging of the Pyrenees and Massif Central from the data of the PYROPE and IBERARRAY portable array deployments. *Journal of Geophysical Research: Solid Earth*, *119*(8), pp.6399-6420. https://doi.org/10.1002/2014JB010953 de Lis Mancilla, F. and Diaz, J., 2015. High resolution Moho topography map beneath Iberia and Northern Morocco from receiver function analysis. *Tectonophysics*, *663*, pp.203-211. https://doi.org/10.1016/j.tecto.2015.06.017

De Vicente, G. and Vegas, R., 2009. Large-scale distributed deformation controlled topography along the western Africa–Eurasia limit: Tectonic constraints. *Tectonophysics*, *474*(1-2), pp.124-143. doi:10.1016/j.tecto.2008.11.026

Diaz, J., Torné, M., Vergés, J., Jiménez-Munt, I., Martí, J., Carbonell, R., Schimmel, M., Geyer, A., Ruiz, M., García-Castellanos, D. and Alvarez-Marrón, J., 2021. Four decades of geophysical research on Iberia and adjacent margins. *Earth-Science Reviews*, p.103841.

Di Bucci, D., P. Burrato, P. Vannoli, and G. Valensise, 2010. Tectonic evidence for the ongoing Africa-Eurasia convergence in central Mediterranean foreland areas: A journey among long-lived shear zones, large earthquakes, and elusive fault motions, *Journal of Geophysical Research: Solid Earth*, *115*, B12404, doi:10.1029/2009JB006480.

Faccenna, C., Piromallo, C., Crespo-Blanc, A., Jolivet, L., and Rossetti, F., 2004. Lateral slab deformation and the origin of the western Mediterranean arcs, *Tectonics*, 23, TC1012, doi:10.1029/2002TC001488.

Faccenna, C., Becker, T.W., Auer, L., Billi, A., Boschi, L., Brun, J.P., Capitanio, F.A., Funiciello, F., Horvath, F., Jolivet, L., Piromallo, C., Royden, L.H., Rossetti, F., Serpelloni, E., 2014. Mantle dynamics in the Mediterranean. *Reviews of Geophysics*, 52, 283–332. https://doi.org/10.1002/2013RG000444

Feng, L. and Ritzwoller, M.H., 2017. The effect of sedimentary basins on surface waves that pass through them, *Geophysical Journal International*, 211(1), 572-592, doi:10.1093/gji/ggx313.

Feng, L., and Ritzwoller, M.H., 2019. A 3-D shear velocity model of the crust and uppermost mantle beneath Alaska including apparent radial anisotropy, *Journal of Geophysical Research: Solid Earth*, 124, 19,468-10,497, doi.org/10.1029/2019JB018122.

Feng, L., Liu, C. and Ritzwoller, M.H., 2020. Azimuthal Anisotropy of the Crust and Uppermost Mantle beneath Alaska. *Journal of Geophysical Research: Solid Earth*, *125*(12), p.e2020JB020076.

Feng, L. 2021. High-resolution crustal and uppermost mantle structure beneath central Mongolia from Rayleigh waves and receiver functions. *Journal of Geophysical Research: Solid Earth*, 126, e2020JB021161. *https://doi.org/10.1029/2020JB021161*

Fernandez, M., C. Almeida, and J. Cabal 1995, Heat flow and heat production in western Iberia, in World Geothermal Congress, edited by E. Barbier, pp. 745–749, International Geotherma Association, Florence.

Fullea, J., M. Fernandez, J. C. Afonso, J. Verg es, and H. Zeyen 2010, The structure and evolution of the lithosphere-asthenosphere boundary beneath the Atlantic-Mediterranean Transition Region, Lithos, 120(1–2), 74–95, doi:10.1016/j.lithos.2010.03.003

Granet, M., Wilson, M. and Achauer, U., 1995. Imaging a mantle plume beneath the French Massif Central. *Earth and Planetary Science Letters*, *136*(3-4), pp.281-296. https://doi.org/10.1016/0012-821X(95)00174-B

Hammond, W.C. and Humphreys, E.D., 2000. Upper mantle seismic wave velocity: Effects of realistic partial melt geometries. *Journal of Geophysical Research: Solid Earth*, *105*(B5), pp.10975-10986., doi:10.1029/2000JB900041

Huismans, R.S. and Beaumont, C., 2008. Complex rifted continental margins explained by dynamical models of depth-dependent lithospheric extension. *Geology*, *36*(2), pp.163-166. https://doi.org/10.1130/G24231A.1

Jammes, S., Tiberi, C., and Manatschal, G., 2010, 3D architecture of a complex transcurrent rift system: The example of the Bay of Biscay–Western Pyrenees: Tectonophysics, v. 489, p.

Kaislaniemi, L. and van Hunen, J., 2014. Dynamics of lithospheric thinning and mantle melting by edge-driven convection: Application to Moroccan Atlas mountains. *Geochemistry, Geophysics, Geosystems*, *15*(8), pp.3175-3189, doi:10.1002/2014GC005414.

Karato, S.I., Jung, H., Katayama, I. and Skemer, P., 2008. Geodynamic significance of seismic anisotropy of the upper mantle: New insights from laboratory studies. *Annual Review of Earth and Planetary Sciences*, *36*, pp.59-95.

Kennett B. L. N., Engdahl E. R. and Buland R. 1995. Constraints on seismic velocities in the earth from travel times. *Geophysical Journal International 122*:108-124. https://doi.org/10.1111/j.1365-246X.1995.tb03540.x

Koulali, A., Ouazar, D., Tahayt, A., King, R.W., Vernant, P., Reilinger, R.E., McClusky, S., Mourabit, T., Davila, J.M. and Amraoui, N., 2011. New GPS constraints on active deformation along the Africa–Iberia plate boundary. *Earth and Planetary Science Letters*, *308*(1-2), pp.211-217. https://doi.org/10.1016/j.epsl.2011.05.048

Lagabrielle, Y., Labaume, P., and de Saint Blanquat, M., 2010, Mantle exhumation, crustal denudation, and gravity tectonics during Cretaceous rifting in the Pyrenean realm (SW Europe): Insights from the geological setting of the lherzolite bodies: Tectonics, v. 29, TC4012, doi:10.1029/2009TC002588.

Laske, G., Masters., G., Ma, Z. and Pasyanos, M., 2013. Update on CRUST1.0 - A 1-degree Global Model of Earth's Crust, *Geophysical Research Abstracts, 15,* Abstract EGU2013-2658.

Laville, E., A. Pique, M. Amrhar, and M. Charroud, 2004. A restatement of the Mesozoic Atlasic Rifting (Morocco), *Journal African Earth Sciences, 38*, 145– 153, doi:10.1016/j.jafrearsci.2003.12.003.

Levander, A. et al. 2014, Subduction-driven recycling of continental margin lithosphere, Nature, 515(7526), 253–256, doi:10.1038/ nature13878.

Ligorria, J.P. and Ammon, C.J., 1999. Iterative deconvolution and receiver-function estimation. *Bulletin of the seismological Society of America*, *89*(5), pp.1395-1400.

Lin, F.C., Ritzwoller, M.H. and Snieder, R., 2009. Eikonal tomography: surface wave tomography by phase front tracking across a regional broad-band seismic array. *Geophysical Journal International*, *177*(3), 1091-1110. https://doi.org/10.1111/j.1365-246X.2009.04105.x

Lin, F.C. and Ritzwoller, M.H., 2011. Helmholtz surface wave tomography for isotropic and azimuthally anisotropic structure. *Geophysical Journal International*, *186*(3), pp.1104-1120. https://doi.org/10.1111/j.1365-246X.2011.05070.x

Lloyd, G. E., Butler, R. W., Casey, M., & Mainprice, D. 2009. Mica, deformation fabrics and the seismic properties of the continental crust. *Earth and Planetary Science Letters*, *288*(1–2), 320–328. https://doi.org/10.1016/j.epsl.2009.09.035

Lonergan, L. and White, N., 1997. Origin of the Betic-Rif mountain belt. *Tectonics*, *16*(3), pp.504-522.

Michard, A., Soulaimani, A., Hoepffner, C., Ouanaimi, H., Baidder, L., Rjimati, E.C. and Saddiqi, O., 2010. The south-western branch of the Variscan Belt: evidence from Morocco. *Tectonophysics*, *492*(1-4), pp.1-24. https://doi.org/10.1016/j.tecto.2010.05.021

Miller, E. L., & Hudson, T. L. 1991. Mid-Cretaceous extensional fragmentation of the Jurassic-Early Cretaceous compressional orogeny, Alaska. *Tectonics*, *10*(4), 781–796. https://doi.org/10.1029/91TC00044

Miller, M.S., O'Driscoll, L.J., Butcher, A.J. and Thomas, C., 2015. Imaging Canary Island hotspot material beneath the lithosphere of Morocco and southern Spain. *Earth and Planetary Science Letters*, *431*, pp.186-194, doi:10.1016/j.epsl.2015.09.026.

Miller, M. S., & Moresi, L. 2018. Mapping the Alaskan Moho. *Seismological Research Letters*, *89*(6), 2439–2436. https://doi.org/10.1785/ 0220180222

Molnar,P. and Houseman, G.A. 2004. The effects of buoyant crust on the gravitational instability of thickened mantle lithosphere at zones of intracontinental convergence, *Geophysical Journal International*, *158*(3), pp. 1134–1150, https://doi.org/10.1111/j.1365-246X.2004.02312.x

Moschetti, M.P., Ritzwoller, M.H., Lin, F. and Yang, Y., 2010. Seismic evidence for widespread western-US deep-crustal deformation caused by extension. *Nature*, *464*(7290), pp.885-889. https://doi.org/10.1038/nature08951

Montagner, J.P., 2007. Upper mantle structure: Global isotropic and anisotropic elastic tomography. *Treatise on geophysics*, *1*, pp.559-589.

Muñoz-Martín, A., De Vicente, G., Fernández-Lozano, J., Cloetingh, S.A.P.L., Willingshofer, E., Sokoutis, D. and Beekman, F., 2010. Spectral analysis of the gravity and elevation along the western Africa–Eurasia plate tectonic limit: Continental versus oceanic lithospheric folding signals. *Tectonophysics*, *495*(3-4), pp.298-314. https://doi.org/10.1016/j.tecto.2010.09.036

Nolet, G., 1977. The upper mantle under western Europe inferred from the dispersion of Rayleigh modes. *Journal of Geophysics*, *43*(1), pp.265-285.

Palomeras, I., Villaseñor, A., Thurner, S., Levander, A., Gallart, J. and Harnafi, M., 2017. Lithospheric structure of Iberia and Morocco using finite-frequency Rayleigh wave tomography from earthquakes and seismic ambient noise. *Geochemistry, Geophysics, Geosystems*, *18*(5), pp.1824-1840. https://doi.org/10.1002/2016GC006657

Pawlewicz, M.J., Steinshouer, D.W. and Gautier, D.L., 1997. *Map showing geology, oil and gas fields, and geologic provinces of Europe including Turkey* (No. 97-470-I). US Geological Survey.

Platt, J.P. & Vissers, R.L.M., 1989. Extensional collapse of thickened continental lithosphere: a working hypothesis for the Alboran Sea and Gibraltar Arc, *Geology, 17*, 540–543. https://doi.org/10.1130/0091-7613(1989)017%3C0540:ECOTCL%3E2.3.CO;2

Ritzwoller, M.H. and Feng, L., 2019. Overview of pre- and post-processing of ambient noise correlations, In N. Nakata, L. Gualtieri, and A. Fichtner (Eds.), Ambient Seismic Noise (pp. 144-187), Cambridge, *Cambridge University Press,* doi:10.1017/9781108264808.007.

Rosenbaum, R., Lister, G.S., Duboz, C., 2002. Relative motions of Africa, Iberia and Europe during Alpine orogeny. *Tectonophysics, 359*, 117–129. https://doi.org/10.1016/S0040-1951(02)00442-0

Schaefer, J.F., Boschi, L., Becker, T.W. and Kissling, E., 2011. Radial anisotropy in the European mantle: Tomographic studies explored in terms of mantle flow. *Geophysical research letters*, *38*(23). https://doi.org/10.1029/2011GL049687

Schutt, D.L. and Lesher, C.E., 2006. Effects of melt depletion on the density and seismic velocity of garnet and spinel lherzolite. *Journal of Geophysical Research: Solid Earth*, *111*(B5). doi:10.1029/2003JB002950

Shapiro, N. M., Ritzwoller, M. H., Molnar, P., & Levin, V., 2004. Thinning and flow of Tibetan crust constrained by seismic anisotropy. *Science, 305*(5681), 233–236. https://doi.org/10.1126/science.1098276

Shen, W**.**, Ritzwoller, M.H., Schulte-Pelkum, V. and Lin, F.C., 2012. Joint inversion of surface wave dispersion and receiver functions: a Bayesian Monte-Carlo approach. *Geophysical Journal International*, *192*(2),.807-836. https://doi.org/10.1093/gji/ggs050

Spakman, W. and Wortel, R., 2004. A tomographic view on western Mediterranean geodynamics. In *The TRANSMED atlas. The Mediterranean region from crust to mantle* (pp. 31-52). Springer, Berlin, Heidelberg. https://doi.org/10.1007/978-3-642-18919-7_2

Sun, D., M. S. Miller, A. F. Holt, and T. W. Becker 2014, Hot upwelling conduit beneath the Atlas Mountains, Morocco, Geophys. Res. Lett., 41, 8037–8044, doi:10.1002/2014GL061884

Tatham, D.J., Lloyd, G.E., Butler, R.W.H., Casey, M., 2008. Amphibole and lower crustal seismic properties. *Earth and Planetary Science Letters*, *267*, 118–128. https://doi.org/10.1016/j.epsl.2007.11.042

Teixell, A., 1998, Crustal structure and orogenic material budget in the west central Pyrenees, *Tectonics*, *3*, 395–406 https://doi.org/10.1029/98TC00561

Thurner, S., Palomeras, I., Levander, A., Carbonell, R. and Lee, C.T., 2014. Ongoing lithospheric removal in the western Mediterranean: evidence from Ps receiver functions and thermobarometry of Neogene basalts (PICASSO project). *Geochemistry, Geophysics, Geosystems*, *15*(4), pp.1113-1127. https://doi.org/10.1002/2013GC005124

Valera, J.L., Negredo, A.M. and Villaseñor, A., 2008. Asymmetric delamination and convective removal numerical modeling: comparison with evolutionary models for the Alboran Sea region. In *Earth Sciences and Mathematics* (pp. 1683-1706). Birkhäuser Basel. doi:10.1007/s00024-008-0395-8.

van der Voo., 1982. Pre-Mesozoic paleomagnetism and plate tectonics. *Annual Review of Earth and Planetary Sciences*, *10*(1), pp.191-220.

van Hinsbergen, D. J. J., R. L. M. Vissers, and W. Spakman, 2014. Origin and consequences of western Mediterranean subduction, rollback, and slab segmentation, *Tectonics*, *33*, 393–419, doi:10.1002/2013TC003349.

Vergés, J. and Fernàndez, M., 2012. Tethys–Atlantic interaction along the Iberia–Africa plate boundary: The Betic–Rif orogenic system. *Tectonophysics*, *579*, pp.144-172. https://doi.org/10.1016/j.tecto.2012.08.032

Wang, Y., Chevrot, S., Monteiller, V., Komatitsch, D., Mouthereau, F., Manatschal, G., Sylvander, M., Diaz, J., Ruiz, M., Grimaud, F. and Benahmed, S., 2016. The deep roots of the western Pyrenees revealed by full waveform inversion of teleseismic P waves. *Geology*, *44*(6), pp.475-478. https://doi.org/10.1130/G37812.1

Ward, D., K. Mahan, and V. Schulte-Pelkum, 2012, Roles of quartz and mica in seismic anisotropy of mylonites, *Geophysical Journal International*, *190*(2), 1123–1134, doi:10.1111/j.1365-246X.2012.05528.x.

Xie, J., Ritzwoller, M.H., Brownlee, S.J. and Hacker, B.R., 2015. Inferring the oriented elastic tensor from surface wave observations: preliminary application across the western United States. *Geophysical Journal International*, *201*(2), 996-1021. https://doi.org/10.1093/gji/ggv054

Zhang, S., Feng, L. and Ritzwoller, M.H., 2020. Three-station interferometry and tomography: coda versus direct waves. *Geophysical Journal International*, *221*(1), pp.521-541. https://doi.org/10.1093/gji/ggaa046

Zhu, H. and Tromp, J., 2013. Mapping tectonic deformation in the crust and upper mantle beneath Europe and the North Atlantic Ocean. *Science*, *341*(6148), pp.871-875. https://doi.org/10.1126/science.1241335

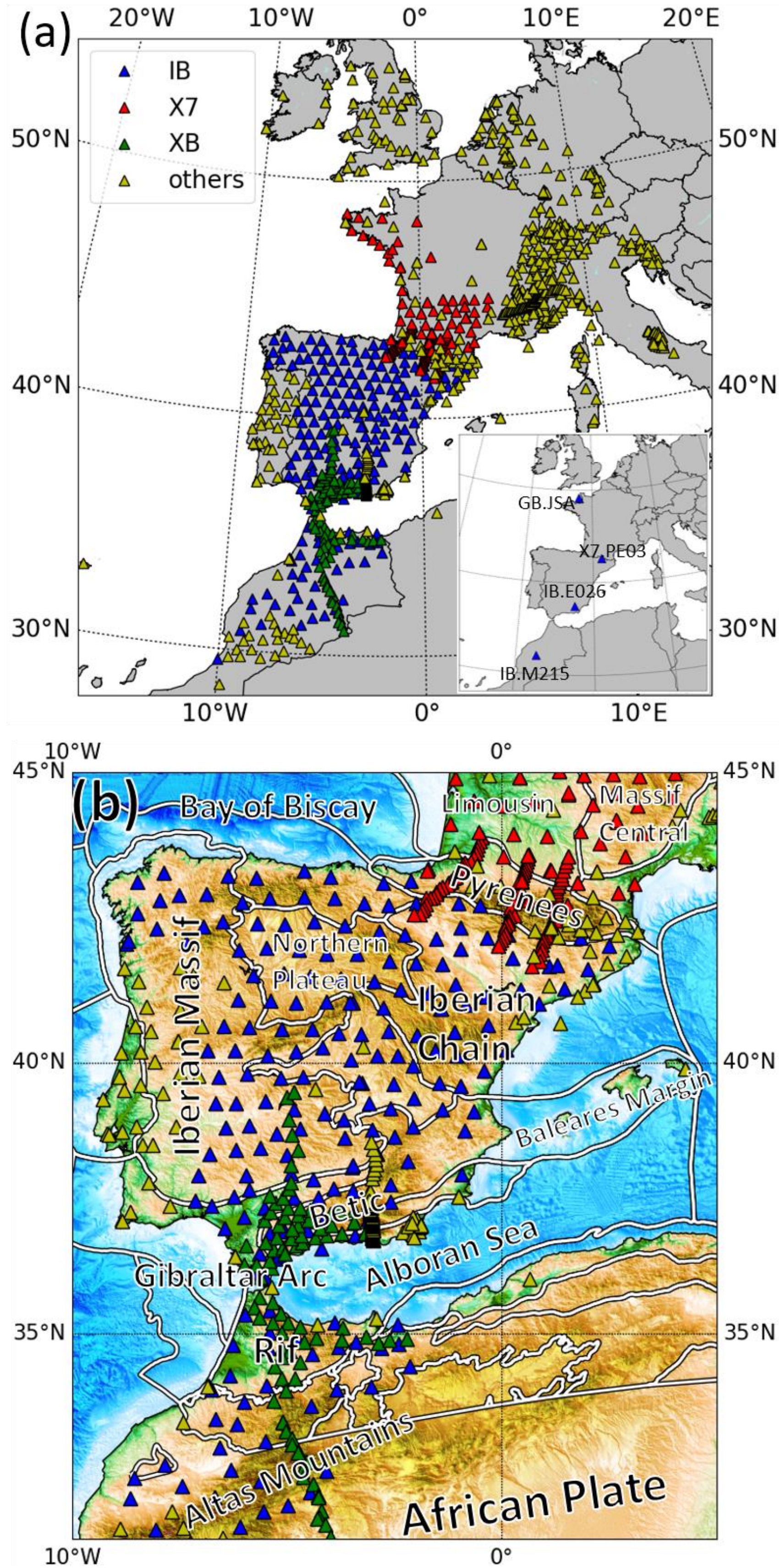
(a)
20°W
10°W
0°
10°E
20°E
IB
X7
XB
others
50°N
40°N
30°N
GB.JSA
X7.PE03
IB.E026
IB.M215
10°W
0°
10°E
(b)
Bay of Biscay
Limousin
Massif
Central
Pyrenees
Northern
Plateau
Iberian Massif
Iberian
Chain
Baleares Margin
Betic
Alboran Sea
Gibraltar Arc
Rif
Altas Mountains
African Plate
45°N
40°N
35°N
10°W
0°

849

Figure 1. (a) Station distribution map. The stations are colored with blue (IB, IberArray), red (X7, PYROPE array), green (XB, PICASSO array) and yellow (other networks). There are in total 1186 stations. The inset map identifies the locations of four sample stations used in **Figure 2** and **Figure S1**. (b) A topographic map of westernmost Mediterranean. White curves with black edges identify major geological provinces (Pawlewicz et al., 1997).

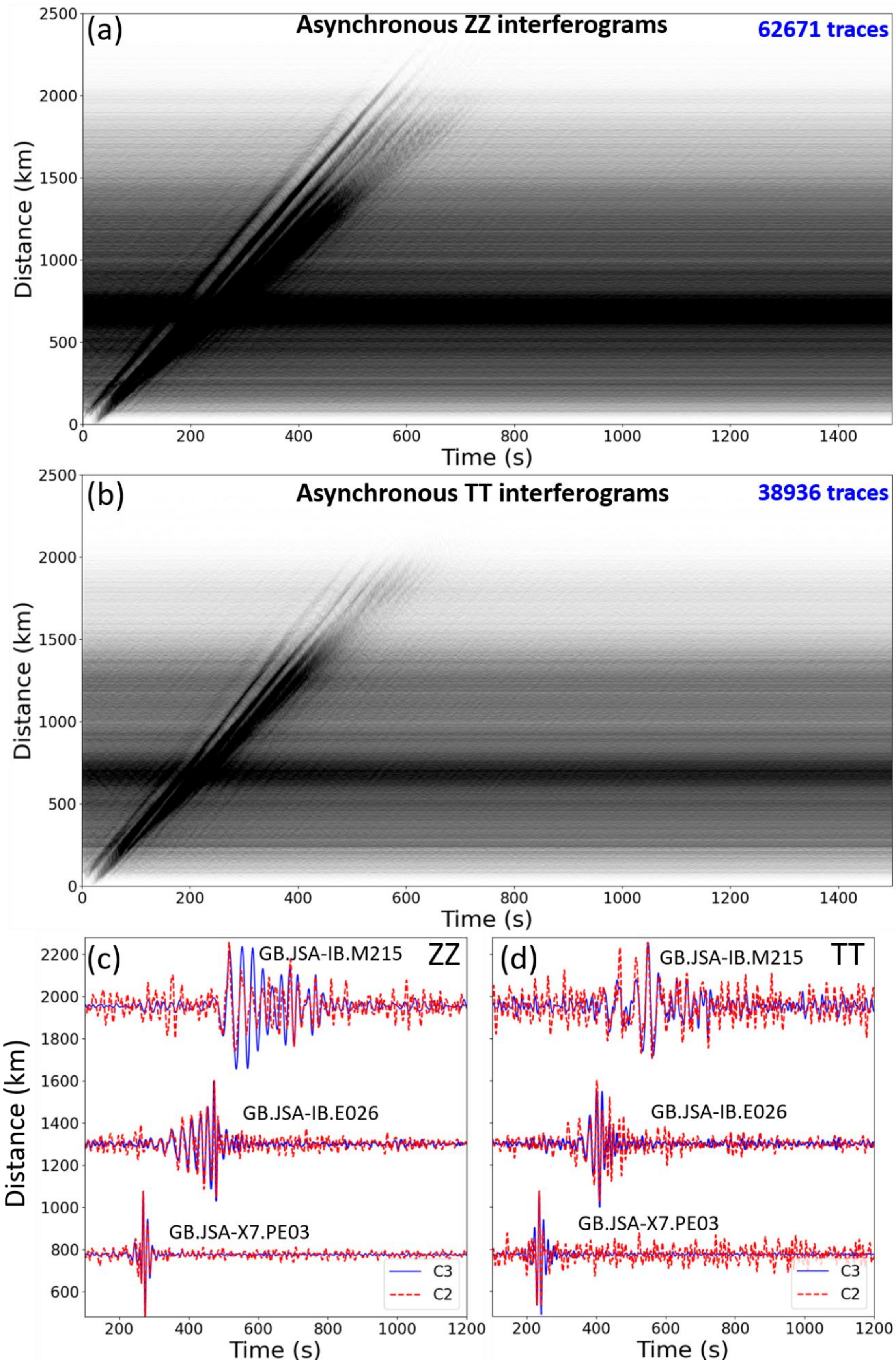
(a)
Asynchronous ZZ interferograms
62671 traces
Distance (km)
Time (s)
(b)
Asynchronous TT interferograms
38936 traces
Distance (km)
Time (s)
(c)
ZZ
GB.JSA-IB.M215
GB.JSA-IB.E026
GB.JSA-X7.PE03
C3
C2
Distance (km)
Time (s)
(d)
TT
GB.JSA-IB.M215
GB.JSA-IB.E026
GB.JSA-X7.PE03
C3
C2
Time (s)

856

Figure 2. (a) Asynchronous three-station interferograms of ZZ component. Each selected station pair includes at least one station belongs to the IB, XB or X7 networks. Number of traces are marked on the figure. (b) Same as (a), but for TT component. (c) Two- and three-station interferograms of ZZ component for three sample station pairs. Amplitudes are normalized in each interferogram. Locations of the sample stations are identified in the inset of **Fig. 1a**. (d) Same as (c), but for TT component.

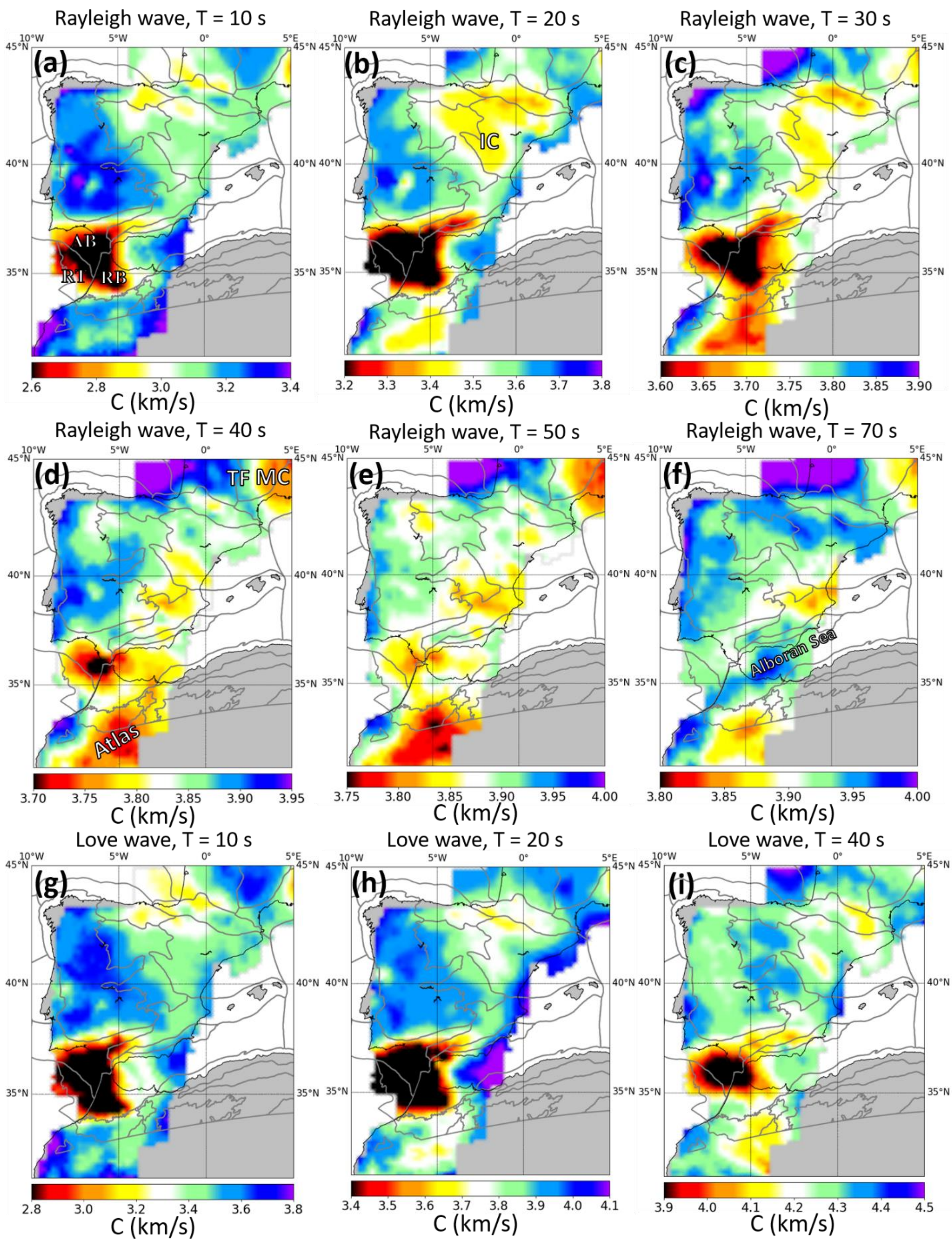

Figure 3. (a) – (f) Example Rayleigh wave phase velocity maps for T = 10 ~ 70 s periods. (g)-(i) Sample Love wave phase speed maps for T = 10 ~ 40 s periods. The grey curves identify major

geological provinces (Pawlewicz et al., 1997). The locations of the Alentejo-Guadalquivir Basin (AB), the Rabat Basin (RB) and the Rif Basin (RB) are identified in (a). In (b): IC: Iberian Chain. In (c) TF: Toulouse Fault; MC: Massif Central.

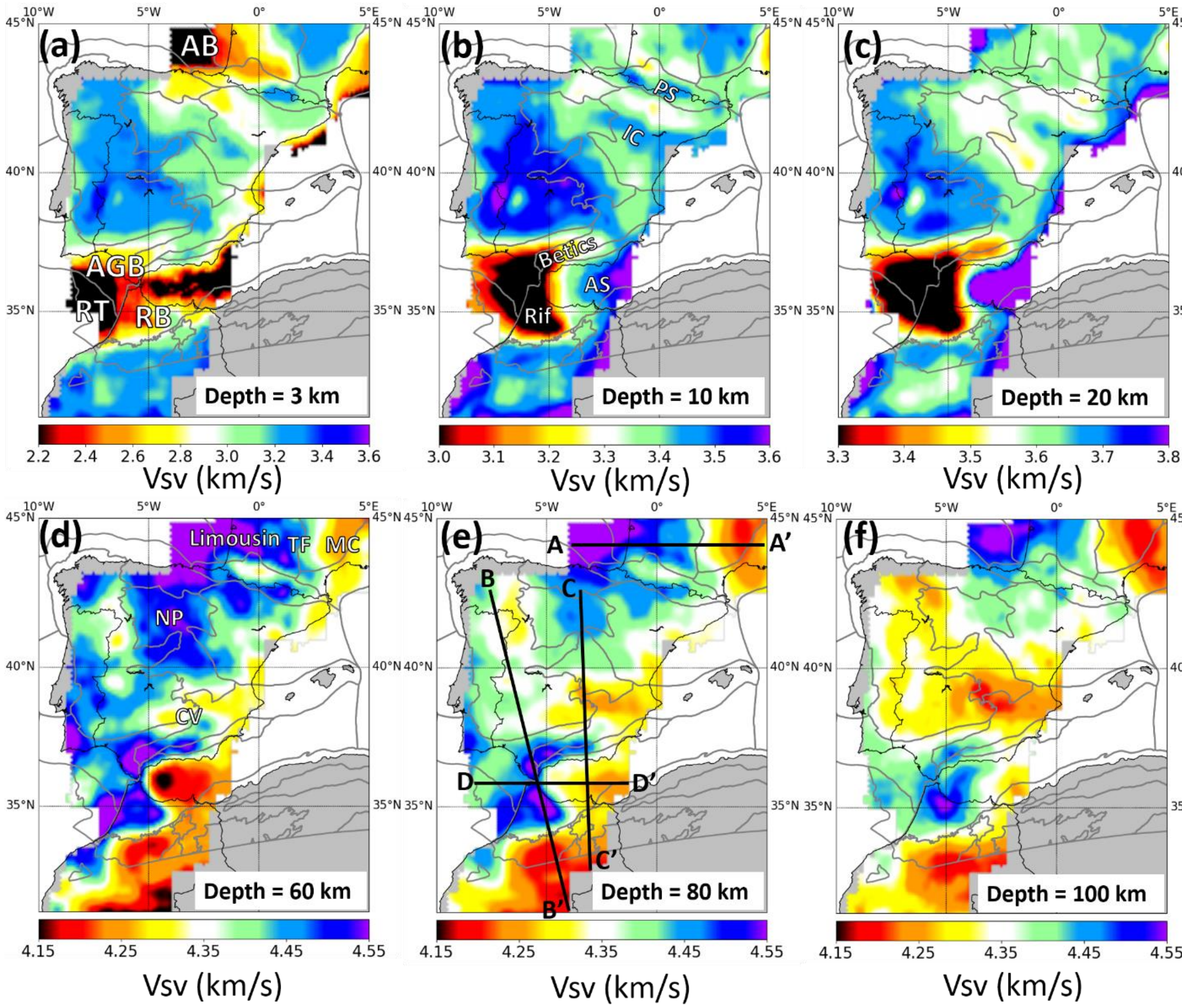

Figure 4. Sample Vsv slices at the depth of 3 km, 10 km, 20 km, 60 km, 80 km and 100 km (central-depth $\pm$ 3 km). In (a), major sedimentary basins are identified with abbreviations: AB: Aquitaine Basin; AGB: Alentejo-Guadalquivir Basin; RT: Rabat Basin; RB: Rif Basin. In (b), PS: Pyrenees; IC: Iberian Chain; AS: Alboran Sea. In (d), MC: Massif Central; TF: Toulouse Fault; NP: Northern Plateau. CV: Calatrava Volcanic field. In (e), locations of the vertical Vsv cross-sections shown in **Figure 8** are marked.

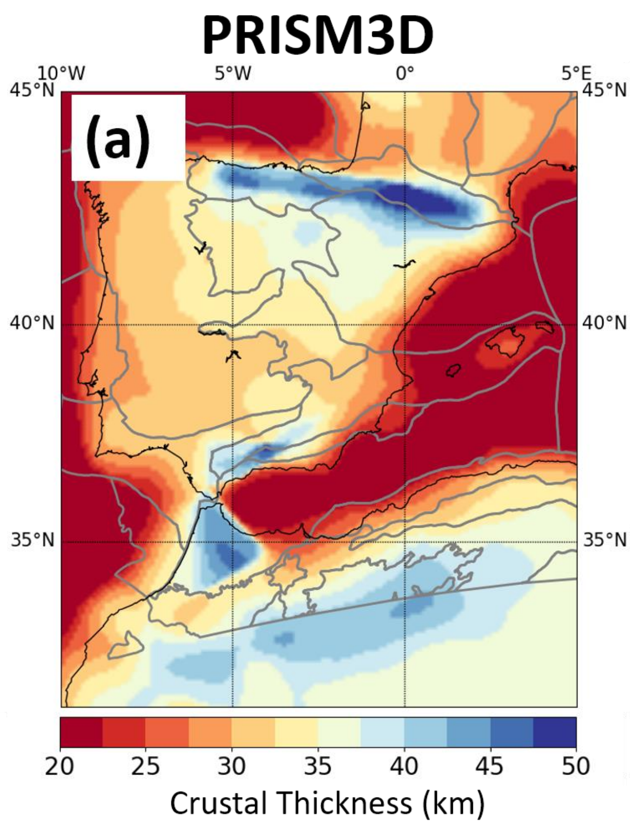

Figure 5. (a) PRISM3D model. (b) Crustal thickness map constructed from this study.

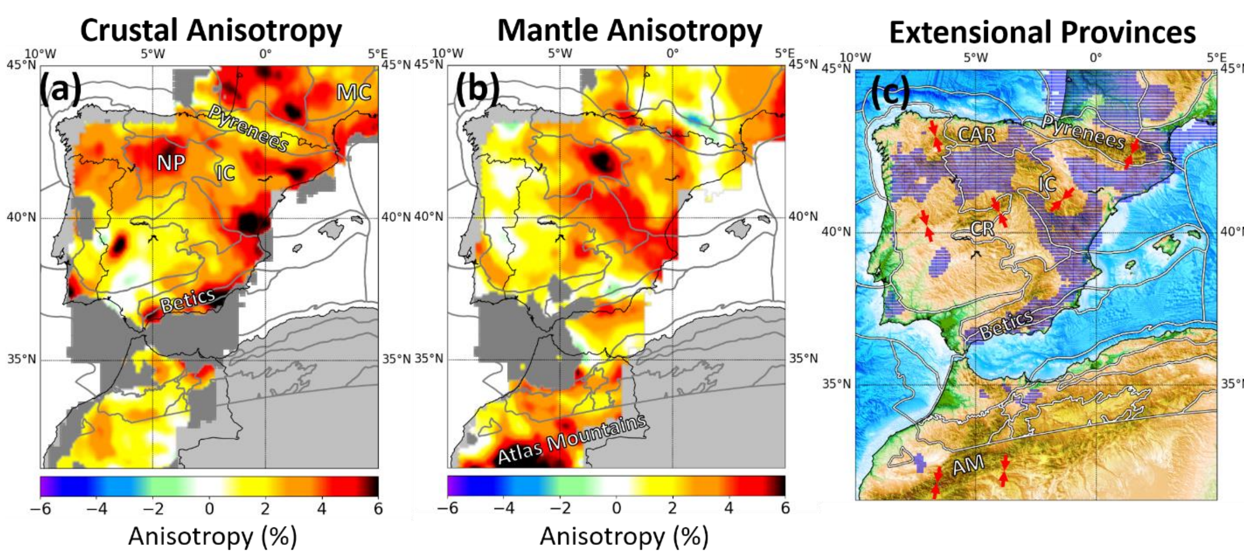

Figure 6. (a) Radial anisotropy in the crust. IC: Iberian Chain, NP: Northern Plateau, MC: Massif Central. (b) Radial anisotropy in the mantle. Grid points with indeterminate value of anisotropy are not shown and colored in grey. (c) Regions (colored in blue) identified with strong anisotropy

in the crust. Red arrows denote regions experienced shortening from the early Oligocene to the lower Miocene, including Pyrenees, the Iberian Chain, the Central Range, the Cantabrian Range and the Atlas Mountains. In (c): AM: Atlas Mountains; CAR: Cantabrian Range; CR: Central Range; IC: Iberian Chain.

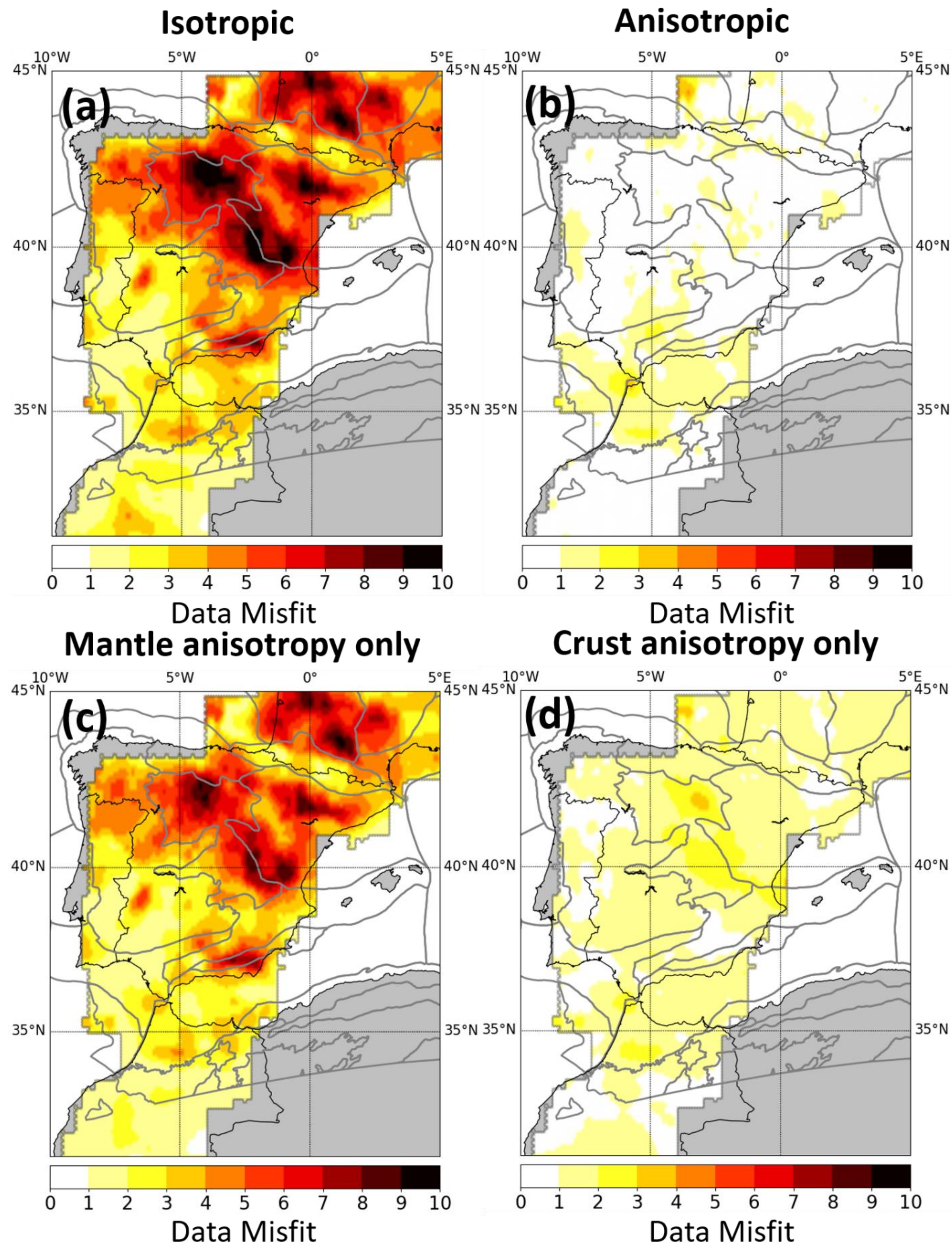
Isotropic
Anisotropic
(a)
(b)
Mantle anisotropy only
Crust anisotropy only
(c)
(d)
10°W
5°W
0°
5°E
45°N
40°N
35°N
0 1 2 3 4 5 6 7 8 9 10
Data Misfit

900

Figure 7. Misfit maps for different models. (a) Isotropic model. (b) Two-layer anisotropic model. (c) Model with anisotropy confined in the mantle only. (d) Model with anisotropy confined in the crust only.

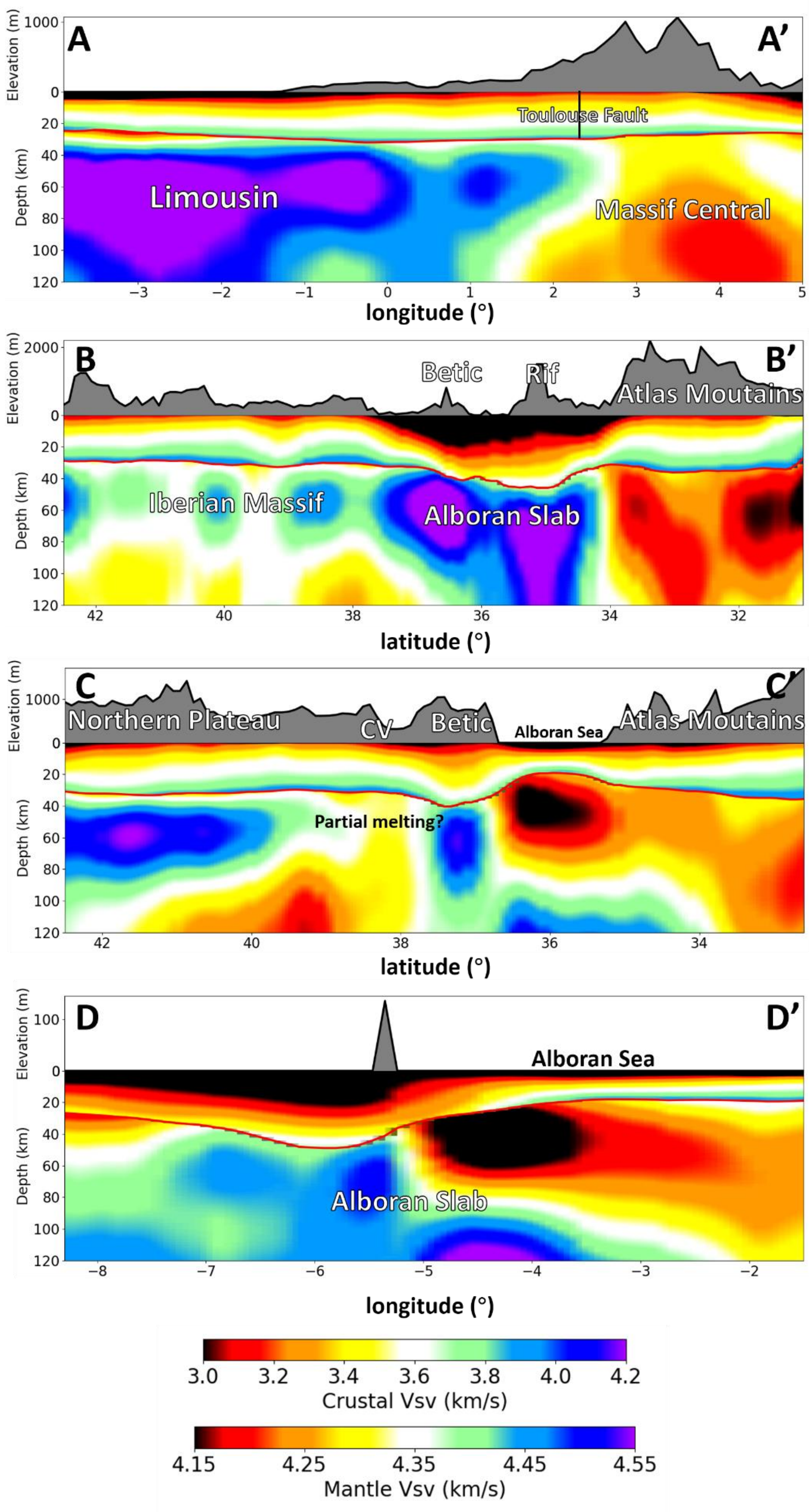

A
A'
Elevation (m)
Depth (km)
Toulouse Fault
Limousin
Massif Central
longitude (°)
B
B'
Betic
Rif
Atlas Moutains
Iberian Massif
Alboran Slab
latitude (°)
C
C'
Northern Plateau
CV
Betic
Alboran Sea
Atlas Moutains
Partial melting?
latitude (°)
D
D'
Alboran Sea
Alboran Slab
longitude (°)
Crustal Vsv (km/s)
Mantle Vsv (km/s)

Figure 8. *Vertical Vsv cross section A–A′, B–B′, C–C′ and D-D′ identified in* ***Figure 4e****. (A–A′) Vsv cross section going through the Limousin and Massif Central. (B–B′) Vsv cross section going through the Iberian Massif, the Gibraltar Arc and the Atlas Mountains. (C–C′) Vsv cross section going through Northen Pleteau, the Betics, the Alboran Sea and the Atlas Mountains. (D–D′) W-E direction Vsv cross section going through the Gibraltar Arc.*